Journal of Computer-Aided Molecular Design (2026) 40:1
https://doi.org/10.1007/s10822-025-00707-z

CORRESPONDENCE

Design, synthesis, pharmacological evaluation and computational modeling of 4-formyl-2-nitrophenyl quinoline-8-sulfonate derived thiosemicarbazones as antidiabetic agents

Muhammad Tayyab[1] · Khalid Mahmood[1] · Khawar Abbas[1] · Farhan Siddique[2] · Nastaran Sadeghian[3] · Halil Şenol[4] · Maryam Bashir[2] · Parham Taslimi[3] · Abdullah K. Alanazi[5] · Mostafa A. Ismail[6] · Xianliang Zhao[7] · Zahid Shafiq[1]

Received: 9 September 2025 / Accepted: 31 October 2025

Abstract

A novel series of thiosemicarbazone derivatives **6(a–i)**, synthesized from 4-formyl-2-nitrophenyl quinoline-8-sulfonate, was evaluated for its antidiabetic potential. Among them, compound **6i** (IC_{50} = 54.51 ± 0.84 µM) displayed the most potent α-glucosidase inhibition, whereas **6e** (IC_{50} = 9.66 ± 0.14 µM) exhibited superior α-amylase inhibition, indicating their dual therapeutic potential against key carbohydrate-hydrolyzing enzymes implicated in postprandial hyperglycemia. These derivatives showed structural diversity with potent and selective inhibition profiles. Structure-activity relationship analysis revealed that electron-withdrawing substituents enhanced enzyme affinity and biological activity. However, molecular docking studies demonstrated strong binding affinities for compounds **6f** and **6b** with docking scores of −9.1 to −10.4 kcal/mol against target proteins, via hydrogen bonding and π–π interactions with catalytic residues. Furthermore, in-silico ADMET evaluation predicted good oral bioavailability, low toxicity, and favorable pharmacokinetic properties. The Density Functional Theory (DFT) calculations supported experimental results, where studied compounds showed lower HOMO-LUMO energy gaps (2.41–3.42 eV), suggesting their significant chemical reactivity and molecular stability of these compounds. Overall, in-vitro and in-silico studies revealed that compounds **6b**, **6f**, **6e**, and **6i** emerged as promising lead molecules for developing dual-action therapeutic agents targeting hyperglycemia and oxidative damage in diabetes management.

Keywords 4-Formyl-2-nitrophenyl quinoline-8-sulfonate · A-amylase · A-glucosidase · Thiosemicarbazone · Molecular docking

✉ Khalid Mahmood
kmchemist@yahoo.com

✉ Farhan Siddique
drfarhansiddique@bzu.edu.pk

✉ Zahid Shafiq
zahidshafiq@bzu.edu.pk

[1] Institute of Chemical Sciences, Bahauddin Zakariya University, Multan 60800, Pakistan

[2] Department of Pharmaceutical Chemistry, Faculty of Pharmacy, Bahauddin Zakariya University, Multan 60800, Pakistan

[3] Department of Biotechnology, Faculty of Science, Bartin University, 74110 Bartin, Turkey

[4] Department of Pharmaceutical Chemistry, Faculty of Pharmacy, Bezmialem Vakif University, 34093 Fatih, İstanbul, Turkey

[5] Department of Chemistry, College of Science, Taif University, Taif, Saudi Arabia

[6] Department of Chemistry, Faculty of Science, Research Center for Advanced Materials Science (RCAMS), King Khalid University, P.O. Box 960, 61421 Abha, Saudi Arabia

[7] School of Biological and Chemical Engineering, Zhejiang University of Science and Technology, Hangzhou 310023, Zhejiang Province, China

Published online: 25 November 2025

Introduction

Diabetes mellitus (DM) is a chronic disorder marked by persistently high blood sugar levels [1, 2]. According to a 2019 global survey by the World Health Organization (WHO), diabetes was the ninth major cause of death and is projected to rank seventh by 2030 [3]. Insulin, produced by pancreatic β-cells, regulates blood glucose and energy metabolism. Its deficiency causes hyperglycemia, leading to complications such as obesity, blindness, hypertension, and kidney failure [4, 5].

Diabetes is broadly classified into two main types: Type 1 and Type 2 [6]. Type 1 diabetes, also called insulin-dependent diabetes, is one of the most prevalent disorders in childhood [7]. Type 2 diabetes is often regarded as a preventable condition. Managing it involves making dietary and lifestyle changes to regulate blood glucose levels. This can be achieved by promoting insulin secretion with the help of drugs and inhibiting the digestion of dietary starch to reduce the sugar absorption process in the small intestine [8].

There are several approaches for the management of diabetes, including the anti-ferroptotic effect observed with quercetin [9, 10], the downregulation of intracellular adhesion molecule-1 (ICAM-1) [11] and decreasing oxidative stress to prevent diabetic complications [12]. However, an effective way to control type 2 diabetes is by suppressing α-glucosidase [13, 14], an enzyme present in the small intestine. This enzyme hydrolyzes 1,4-linked α-D-glucose, releasing α-glucose, which increases postprandial blood sugar levels. Clinically approved α-glucosidase inhibitors, acarbose, miglitol, and voglibose, are used in diabetes management [15]. In addition to their antidiabetic activity, these compounds have potential as anti-cancer agents [16], and anti-hepatitis agents [17].

α-Amylase is a calcium-containing endoenzyme that assists in digestion by breaking α-(1, 4)-D-glycosidic linkages in starch and other polysaccharides to produce glucose and maltose [18–20]. Glucose fragments absorbed in the small intestine elevate blood sugar levels, which is responsible for diabetes, obesity, nephropathy, and dental disorders [21]. The α-amylase inhibitors, such as voglibose and miglitol, have been used to reduce blood glucose levels. These inhibitors may lead to gastrointestinal issues such as diarrhea, abdominal pain, and dyspepsia [22].

Thiosemicarbazones have emerged as a significant class of N, S-donor ligands, recognized for their versatile donor abilities, scaffold diversity, and extensive biological applications [8]. They are imine derivatives containing CS and NH functional groups that coordinate with metal ions [23]. Extensive research has reported their biological activities, including anticancer [24, 25], antimalarial [26], antiviral [27], antibacterial [21], antifungal [22], antimicrobial [18], antioxidant [19, 28], and anti-diabetic [29–35] and anti-cholinesterase activity [36, 37]. Several derivatives have shown potent inhibition against key metabolic enzymes, such as α-amylase and α-glucosidase, with IC_{50} values ranging from 3.18 ± 1.72 to 9.53 ± 0.29 μM, surpassing the standard acarbose (IC_{50} = 21.55 ± 1.31 μM). Similarly, strong antioxidant activity has been reported with hydroxyl radical scavenging IC_{50} values between 25.85 ± 1.13 and 58.9 ± 2.95 μM, outperforming vitamin C (IC_{50} = 60.51 ± 1.02 μM) [29–31]. Moreover, thiosemicarbazone derivatives have demonstrated significant acetylcholinesterase and butyryl-cholinesterase inhibition, with IC_{50} values ranging from 41.51 ± 3.88 to 95.48 ± 0.70 μM and 64.47 ± 2.74 to 80.62 ± 0.73 μM, respectively, exceeding galantamine (IC_{50} = 104.5 ± 1.20 μM) [36, 37]. These findings, supported by molecular docking and DFT analyses, highlight the strong binding affinity and favorable electronic characteristics of thiosemicarbazones, emphasizing their therapeutic potential as multifunctional agents against diabetes, oxidative stress, and neurodegenerative disorders. Numerous studies have reported a diverse array of effective inhibitors for α-amylase and α-glucosidase, as shown in Fig. 1 [35, 38–42].

Aryl sulfonates, considered valuable building blocks in medicinal chemistry, are prepared by reacting phenolic compounds with sulfonyl chlorides [43, 44]. These compounds exhibit diverse biological activities, including anticancer [45], antioxidant [46], and carbonic anhydrase properties [47].

The design of dual-target drugs has garnered considerable interest in recent years, emerging as a fast-growing area of interest for medicinal chemists. Recognizing the biological potential of thiosemicarbazone-containing compounds, we were encouraged to synthesize and evaluate their inhibitory effects against α-amylase and α-glucosidase [29]. Through a systematic screening process, we aim to investigate the inhibitory potential of these derivatives and explore their therapeutic prospects for managing hyperglycemia. The findings of this study may contribute to improved diabetes management strategies and support the development of novel antidiabetic drugs [35]. We present the synthesis of 4-formyl-2-nitrophenyl quinoline-8-sulfonate-derived thiosemicarbazones by the incorporation of 4-formyl-2-nitrophenyl quinoline-8-sulfonate with thiosemicarbazide derivatives.

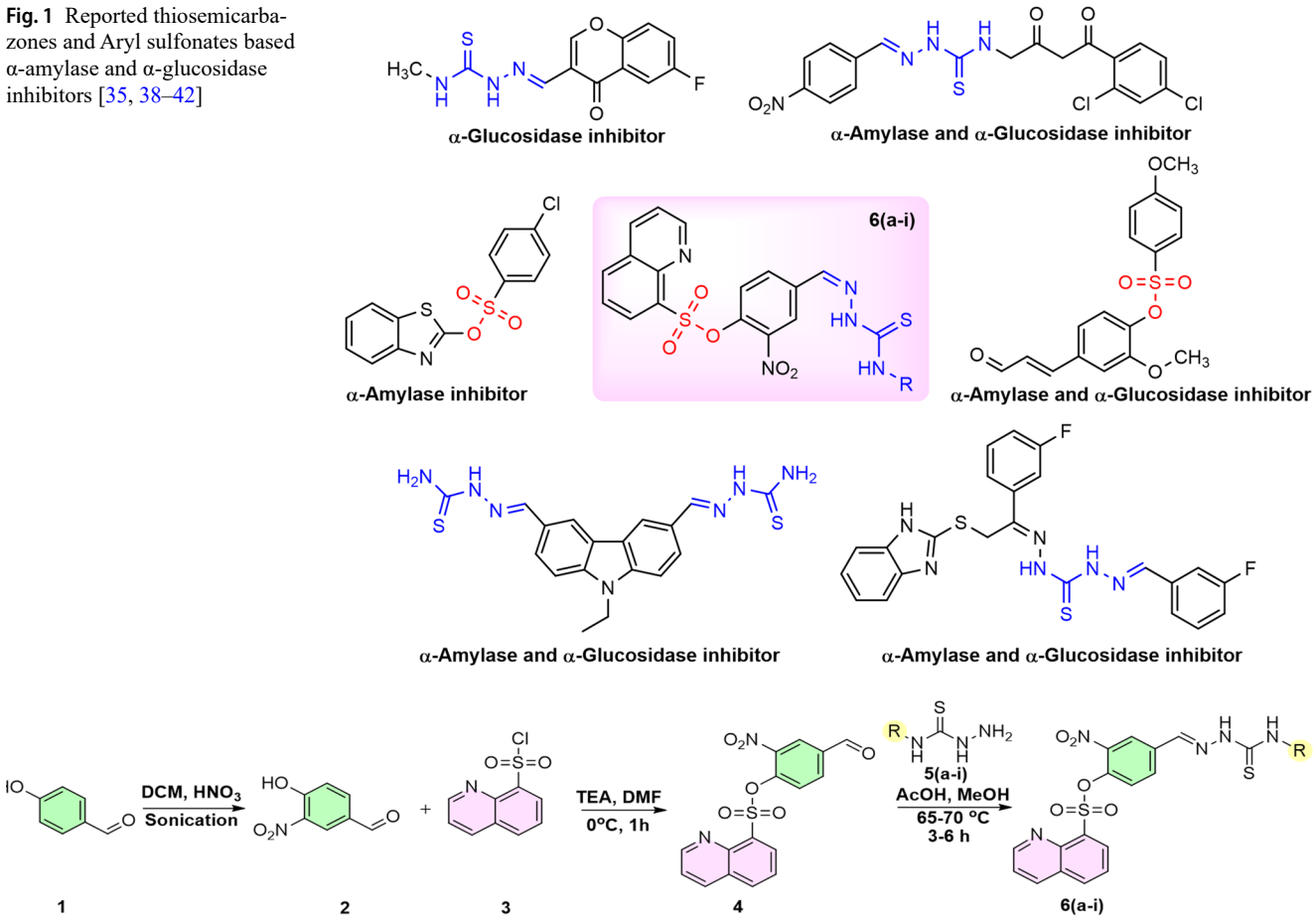

Fig. 1 Reported thiosemicarbazones and Aryl sulfonates based α-amylase and α-glucosidase inhibitors [35, 38–42]

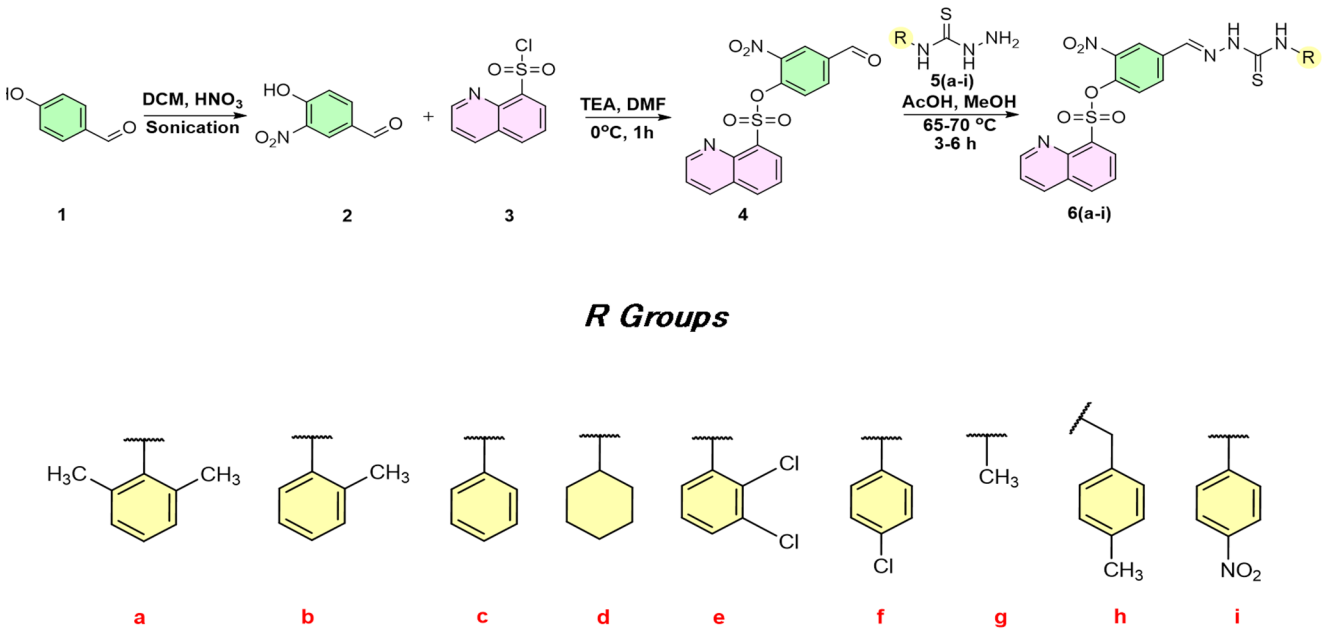

Scheme 1 Synthesis of thiosemicarbazone derivatives 6(a-i)

Results and discussion

Chemistry

4-Hydroxybenzaldehyde and thiosemicarbazones are known for their diverse biological and pharmacological activities. Integrating both moieties into one structural scaffold is a promising strategy for designing potent antidiabetic agents Fig. 1. Compounds **6(a-i)** are synthesized by substituting the hydroxyl group in 4-hydroxybenzaldehyde. The process involved sonicating 4-hydroxybenzaldehyde **(1)** with nitric acid in the presence of DCM, yielding 4-hydroxy-3-nitrobenzaldehyde **(2).** Compound **(2)** is reacted with Quinoline-8-sulfonyl chloride **(3)** using DMF and TEA at 0 °C for 1 h, producing 4-formyl-2-nitrophenyl quinoline-8-sulfonate **(4).** Thiosemicarbazones **6(a-i)** are prepared by reacting 4-formyl-2-nitrophenyl quinoline-8-sulfonate **(4)** with thiosemicarbazides **5(a-i)**. The pathway for the synthesis of 4-formyl-2-nitrophenyl quinoline-8-sulfonate-derived thiosemicarbazones **6(a-i)** is displayed in Scheme 1.

Table 1 IC_{50} and R^2 values of novel compounds against α-amylase and α-glucosidase

Codes	IC_{50} (μM)				Ki (μM)
	α-Glu	R^2	α-Amylase	R^2	α-Glu
6a	113.56 ± 0.93	0.922	23.82 ± 0.05	0.939	122.07 ± 3.57
6b	118.32 ± 0.40	0.954	29.01 ± 0.12	0.950	129.34 ± 2.52
6c	155.68 ± 0.98	0.963	28.46 ± 0.05	0.957	172.16 ± 4.68
6d	169.71 ± 0.31	0.925	25.20 ± 0.43	0.966	178.47 ± 5.13
6e	55.20 ± 0.74	0.907	9.66 ± 0.14	0.909	57.29 ± 3.64
6f	73.65 ± 1.01	0.942	18.43 ± 0.08	0.987	80.67 ± 4.50
6g	128.66 ± 0.36	0.977	35.67 ± 0.22	0.937	139.30 ± 2.62
6h	107.34 ± 0.45	0.970	33.07 ± 0.71	0.901	150.09 ± 3.15
6i	54.51 ± 0.84	0.983	12.68 ± 0.04	0.993	58.79 ± 2.77
ACR	117.83 ± 1.04	0.954	30.15 ± 0.30	0.917	148.40 ± 4.89

Biological activity

Compounds **6(a-i)** are prepared and assessed for their anti-diabetic potential. The IC_{50} and r^2 values are described in Table 1. The 4-formyl-2-nitrophenyl quinoline-8-sulfonate **(4)** and thiosemicarbazides **5(a-i)** served as significant structural scaffolds, with the phenyl and sulfonyl groups in the thiosemicarbazide moiety playing a crucial role in defining a specific structure-activity-relationship.

Structure activity relationship

α-glucosidase

SAR analysis revealed that phenyl-substituted derivatives demonstrated notable inhibition against α-glucosidase. Among them, compound **6i** (IC_{50} = 54.51 ± 0.84 μM) bearing a NO_2 group at the *para* position of the phenyl ring exhibited the highest potency. Compound **6e** (IC_{50} = 55.20 ± 0.74 μM) with chloro groups at the *ortho* and *meta* positions exhibited stronger inhibitory activity than **6f** (IC_{50} = 73.65 ± 1.01 μM). All phenyl derivatives with halogen substitutions demonstrated a potent inhibitory effect against α-glucosidase, which may be associated with the negative inductive effect exerted by halogens on the aromatic ring. Compounds **6h** (IC_{50} = 107.34 ± 0.45 μM), **6a** (IC_{50} = 113.56 ± 0.93 μM), **6b** (IC_{50} = 118.32 ± 0.40 μM), and **6g** (IC_{50} = 128.66 ± 0.36 μM) bearing benzyl, dimethyl, and methyl substitutions at the phenyl ring, respectively, exhibited comparatively lower inhibitory activity. This suggested that electron-donating groups may reduce inhibitory activity by donating electron density to the main nucleus. Compound **6c** (IC_{50} = 155.68 ± 0.98 μM), **6d** (IC_{50} = 169.71 ± 0.31 μM) bearing phenyl and cyclohexyl substitutions, also showed weaker inhibition, further supporting the negative impact of electron-donating groups on α-glucosidase inhibitory activity.

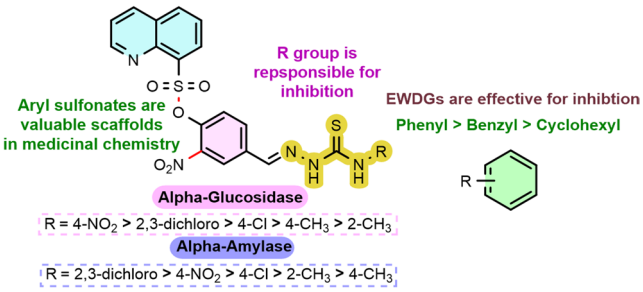

Fig. 2 SAR of the synthesized thiosemicarbazones

α-amylase

SAR analysis revealed that phenyl-substituted derivatives demonstrated notable inhibition against α-amylase. Among them, compound **6e** (IC_{50} = 9.66 ± 0.14 μM) bearing chloro groups at the *ortho* and *meta* positions exhibited the highest potency. Compound **6i** (IC_{50} = 12.68 ± 0.04 μM) with NO_2 substitution exhibited stronger inhibitory activity than **6f** (IC_{50} = 18.43 ± 0.08 μM) with chloro substitution. All phenyl derivatives with halogen substitutions demonstrated a potent inhibitory effect against α-amylase, which may be associated with the negative inductive effect exerted by halogens on the aromatic ring. Compounds **6a** (IC_{50} = 23.82 ± 0.05 μM), **6d** (IC_{50} = 25.20 ± 0.43 μM), **6c** (IC_{50} = 28.46 ± 0.05 μM), and **6b** (IC_{50} = 29.01 ± 0.12 μM), bearing methyl, cyclohexyl, phenyl, and dimethyl substitutions at the phenyl ring, respectively, exhibited moderate inhibitory activity. This suggested that electron-donating groups may decrease inhibitory activity by donating electron density to the main nucleus. Compounds **6h** (IC_{50} = 33.07 ± 0.71 μM), **6g** (IC_{50} = 35.67 ± 0.22 μM), which include benzyl and methyl substitutions, respectively, showed weaker inhibition (Fig. 2).

Molecular docking

The potential anti-diabetic activity of thiosemicarbazone derivatives is assessed in silico by evaluating their inhibitory effects on three key enzymes: α-amylase, α-glucosidase, and aldose reductase. Figure 3 illustrated the superimposition of experimentally determined and re-docked conformations of the co-crystallized ligands within the binding pockets of the target proteins (PDB IDs: 4YU1, 4GQR, and 3L4Y), alongside their respective RMSD values. The computed RMSD values are found to be 1.192 Å, 0.141 Å, and 1.617 Å for target proteins 4YU1, 4GQR, and 3L4Y, respectively, supporting the reliability and accuracy of the docking protocols.

Table 2 summarizes key amino acid residues involved in the binding of top hit compounds with target proteins, highlighting the nature of interactions, bond distances, and binding energies (expressed in kcal/mol). All tested compounds

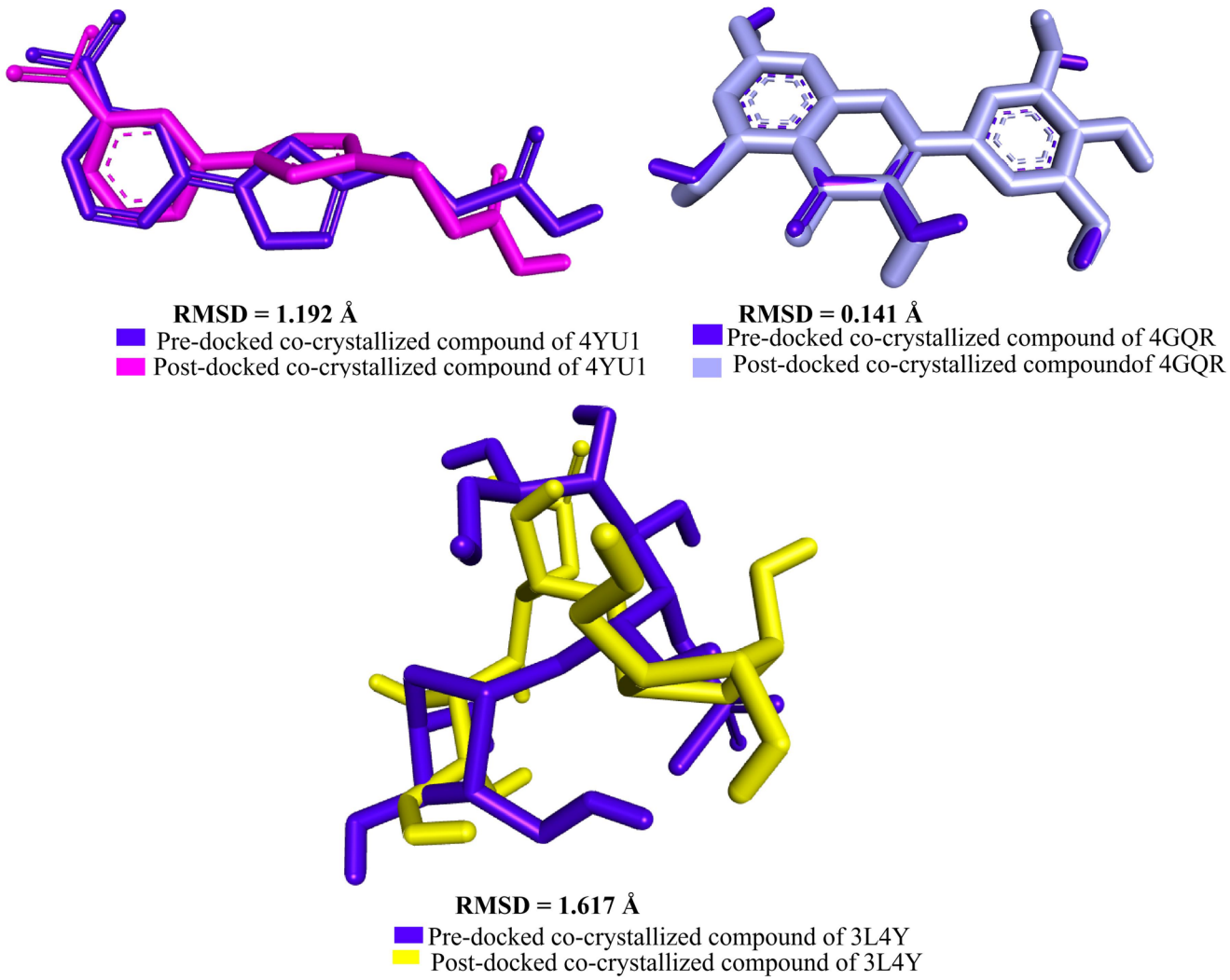

Fig. 3 Overlay of original and re-docked co-crystallized compound with annotated RMSD value for 4YU1, 4GQR, and 3L4Y proteins

demonstrated favorable binding affinities toward their respective targets. The compound **6f** exhibited the strongest binding to 4YU1 and 4GQR, with binding energies of −10.6 and −9.1 kcal/mol, respectively, accompanied by a higher number of interactions. The **6f** formed multiple interactions with 4GQR, including an electrostatic interaction with ASP197 (3.81 Å) and hydrophobic contacts with TYR62, TRP59, and LEU165, with bond distances ranging from 3.98 to 5.39 Å. In contrast, the co-crystallized ligand (myricetin) primarily engaged in hydrophobic contact with PRO4 (4.59 Å) and hydrogen bonds with GLY9, ARG10, ARG252, ARG421, GLN7, THR6, and ASP402, at distances ranging from 1.79 to 3.63 Å. For 4YU1, the compound **6f** exhibited electrostatic and H-bonding interactions with ASP224, PHE311, and ASN294 along with several hydrophobic contacts with TRP219, TRP295, ARG296, and ALA299, with distances between 3.69 and 5.39 Å. However, compound **6b** showed the most significant interaction profile with 3L4Y, recording a binding energy of −9.1 kcal/mol, which is markedly better than its co-crystallized reference compound (−5.6 kcal/mol). Regarding the 3L4Y protein, **6b** established multiple hydrogen bonds with residues ARG647, ARG653, ASP649, and GLY766, with bond lengths between 1.93 and 3.48 Å. Electrostatic interactions are observed with GLU767 and GLU788 (4.06 and 4.93 Å), while a hydrophobic interaction is noted with PRO676 (3.53 Å). The co-crystallized ligand interacted with ARG471 through both hydrogen bonding and electrostatic contacts, and formed hydrogen bonds with ASN14, GLN19, THR196, and PRO17 at distances of 2.48–3.04 Å. The 2D and 3D interaction maps, along with hydrogen bonding surfaces for the top-hit compounds and crystallized ligands, are illustrated in Figs. 4 and 5. The details of docking scores for all studied compounds are provided in Table S1 (Supplementary file).

Table 2 The key interactions and bond distance along with the binding affinity of thiosemicarbazone derivatives with target proteins (PDB ID: 4GQR, 4YU1, and 3L4Y)

Compounds name	Interacting amino acids	Type of interactions	Bond distance (Å)	Binding affinity (Kcal/mol)
4GQR				
6f	ASP197	Electrostatic	3.81	−9.1
	TYR62	Hydrophobic	3.98	
	HIS201	Other	4.49	
	TRP59	Hydrophobic	4.32	
	TRP59	Hydrophobic	5.32	
	TRP59	Hydrophobic	4.27	
	TRP59	Hydrophobic	5.39	
	LEU165	Hydrophobic	5.14	
Co-crystallized	GLY9	H-bond	2.25	−9.1
	ARG10	H-bond	2.44	
	ARG252	H-bond	2.55	
	ARG421	H-bond	2.85	
	ARG421	H-bond	1.79	
	GLN7	H-bond	3.32	
	ARG10	H-bond	2.74	
	THR6	H-bond	3.12	
	ASP402	H-bond	3.63	
	PRO4	Hydrophobic	4.59	
3L4Y				
6b	GLU767	Electrostatic	4.06	−9.1
	ARG647	H-bond	3.06	
	ARG647	H-bond	2.71	
	ARG653	H-bond	1.93	
	ARG653	H-bond	2.22	
	ARG653	H-bond	2.83	
	ASP649	H-bond	3.19	
	GLY766	H-bond	2.25	
	GLY766	H-bond	3.48	
	GLU788	Electrostatic	4.93	
	PRO676	Hydrophobic	3.53	
Co-crystallized	ARG471	H-bond; Electrostatic	2.73	−5.6
	ARG471	H-bond; Electrostatic	2.58	
	ASN14	H-bond	2.54	
	GLN19	H-bond	3.04	
	THR196	H-bond	2.48	
	PRO17	H-bond	2.48	
4YU1				
6f	ASP224	Electrostatic	5.46	−10.4
	PHE311	H-bond	3.59	
	ASN294	H-bond	3.60	
	TRP219	Hydrophobic	3.69	
	TRP219	Hydrophobic	4.81	
	TRP219	Hydrophobic	4.83	
	TRP295	Hydrophobic	4.95	
	TRP295	Hydrophobic	5.28	
	ARG296	Hydrophobic	4.71	
	ALA299	Hydrophobic	5.39	
	ALA299	Hydrophobic	4.92	

Table 2 (continued)

Compounds name	Interacting amino acids	Type of interactions	Bond distance (Å)	Binding affinity (Kcal/mol)
Co-crystallized	GLN183	H-bond	2.31	−7.6
	TRP111	Other	4.94	
	TRP111	Other	5.27	
	HIS110	Hydrophobic	5.06	
	VAL47	Hydrophobic	5.01	
	CYS298	Hydrophobic	4.97	

ADMET analysis

The series of thiosemicarbazone derivative compounds, along with the co-crystallized ligands of targeted proteins, underwent ADMET analysis through the https://lmmd.ecust.edu.cn/admetsar3/resource.php [48]. The prediction module, supported by the CLMGraph framework, was applied to identify the ADME parameters [49]. In silico ADMET analysis identifies the important pharmacokinetic parameters, including TPSA, SlogP, logS, BBB, HIA, P-gp-inhibitor, and CYP-inhibition, which are summarized in Table 3. The TPSA value for all the compounds is < 140 Å² except **6i**, indicating favourable oral bioavailability. All the compounds have acceptable lipophilicity with SlogP < 5 [50]. Compounds exhibiting negative SlogP and logS values are indicative of limited membrane permeability and low aqueous solubility, respectively. Despite these characteristics, they demonstrated favorable intestinal absorption, as reflected by high HIA values ranging between 0.7 and 1. Moreover, these compounds showed the potential to inhibit P-glycoprotein and displayed a moderate capacity to penetrate the blood-brain barrier. All tested compounds acted as inhibitors of the CYP3A4 enzyme, whereas none showed inhibitory activity against CYP2D6.

Quantum computational studies

Optimized geometries

The molecular geometries of a series of selected compounds are optimized to their respective true energy minima confirmed by the absence of imaginary frequencies. The optimized structures are presented in Fig. 6. Among the studied molecules, the optimization energies ranged approximately from −3252.50 to −2141.46 a.u., reflecting variation in molecular size and electronic configuration. Calculated polarizability values varied across the set, with the highest observed around 417.17 a.u. and the lowest near 309.35 a.u., while dipole moments ranged from 3.29 to 11.02 D, indicating differences in molecular polarity. The compound **6b** exhibited significantly higher polarizability (390.95 a.u.) and dipole moment (11.02 D), suggesting its potential for stronger intermolecular interactions and greater responsiveness to external electric fields.

The frontier molecular orbitals commonly referred to as HOMO and LUMO are analyzed for all studied compounds, providing valuable insight into their electronic characteristics and reactivity tendencies. Among the series, the HOMO energies ranged from −5.62 to −6.30 eV, while LUMO levels varied between −2.81 and −3.26 eV, representing a significant electron-accepting property of the studied compounds. The calculated band gap energies spanned from 2.41 to 3.42 eV. Compound **6b** displayed the smallest band gap (2.41 eV), indicating its comparatively high chemical softness and potential for greater chemical reactivity and lower kinetic stability. Conversely, the compound **6h** with the largest energy gap (3.42 eV) is expected to be chemically more stable but less reactive under similar conditions. A summary of the optimized energies, polarizability, and dipole moments, and HOMO/LUMO energies and energy gaps of the studied compounds is listed in Table 4.

The HOMO/LUMO contour maps are illustrated in Fig. 7, where HOMO is mostly located on to thiosemicarbazone moiety. In contrast, the LUMO is centered on the *p-nitrobenzene* moiety. In accordance with Koopmans' theorem, the negative of the HOMO energy approximates the ionization potential (I), while the negative of the LUMO energy represents the electron affinity (A). These values were further used to determine key global reactivity descriptors, namely: chemical hardness ($\eta = (I - A)/2$), softness ($S = 1/2\eta$), chemical potential ($\mu = -(I+A)/2$), and the electrophilicity index ($\omega = \mu^2/2\eta$) [51].

For the most reactive compound **6b**, the ionization potential and electron affinity were found to be around 5.62 eV and 3.21 eV, respectively, resulting in a low hardness ($\eta \approx 1.20$ eV) and a high electrophilicity index ($\omega \approx 8.09$ eV). On the other hand, the least reactive compound **6h** displayed a greater hardness value ($\eta \approx 1.71$ eV) and a significantly lower electrophilicity index ($\omega \approx 5.98$ eV), supporting its inert nature. The values of derived reactivity parameters are compiled and presented in Table 5 for comparison across the full set of compounds.

The MEP surface offers a useful way to identify regions that are likely to participate in chemical reactions, especially in the context of hydrogen bonding and biological

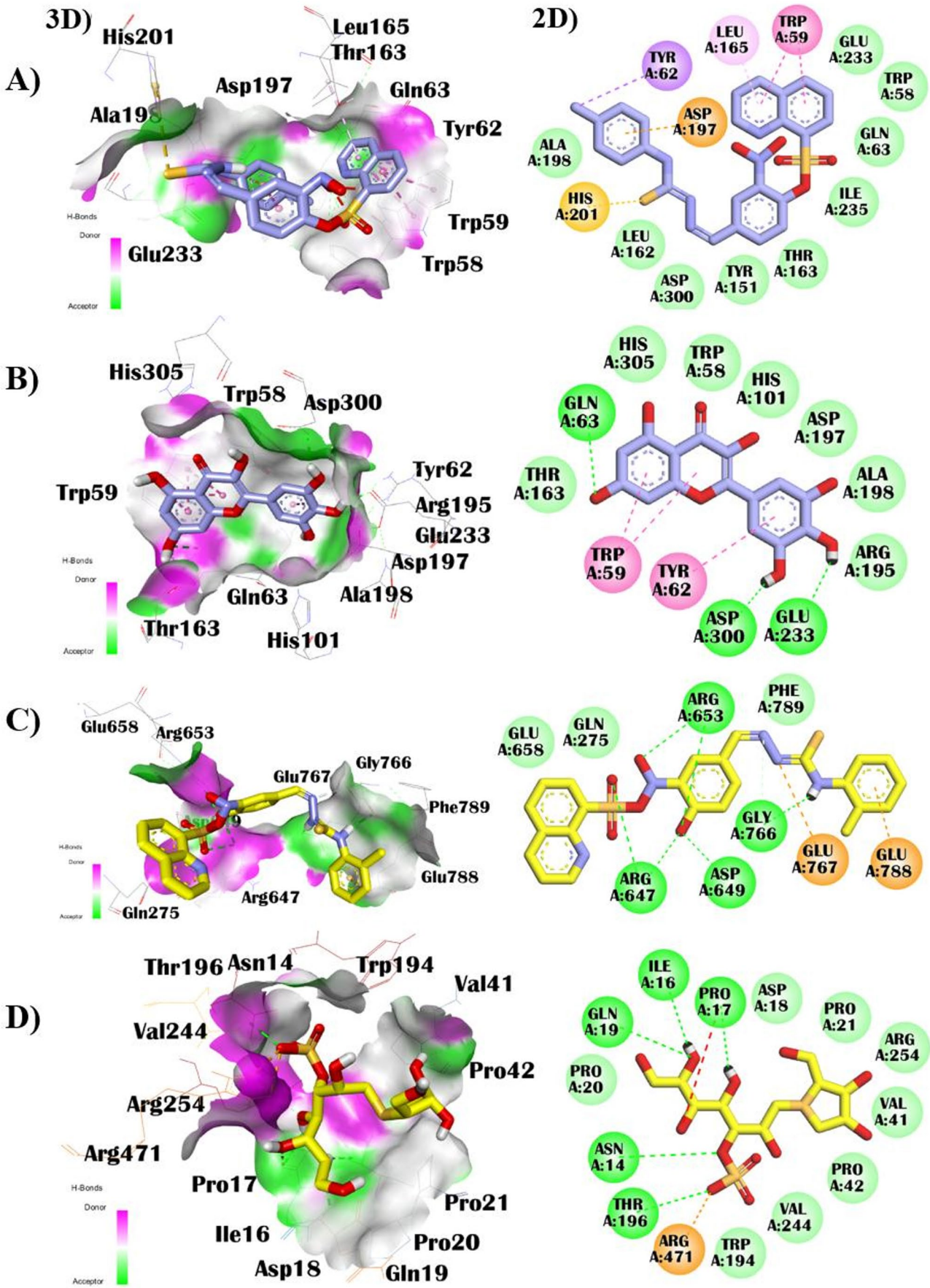
3D)
2D)
A)
His201
Leu165
Thr163
Asp197
Gln63
Ala198
Tyr62
Trp59
Glu233
Trp58
H-Bonds
Donor
Acceptor
TRP A:59
LEU A:165
GLU A:233
TYR A:62
TRP A:58
ASP A:197
GLN A:63
ALA A:198
HIS A:201
ILE A:235
LEU A:162
THR A:163
ASP A:300
TYR A:151
B)
His305
Trp58
Asp300
Tyr62
Trp59
Arg195
Glu233
Asp197
Gln63
Ala198
Thr163
His101
HIS A:305
TRP A:58
HIS A:101
GLN A:63
ASP A:197
THR A:163
ALA A:198
TRP A:59
TYR A:62
ARG A:195
ASP A:300
GLU A:233
C)
Glu658
Arg653
Glu767
Gly766
Phe789
Glu788
Arg647
Gln275
ARG A:653
PHE A:789
GLU A:658
GLN A:275
GLY A:766
GLU A:767
GLU A:788
ARG A:647
ASP A:649
D)
Thr196
Asn14
Trp194
Val41
Val244
Pro42
Arg254
Arg471
Pro17
Pro21
Ile16
Pro20
Asp18
Gln19
ILE A:16
PRO A:17
ASP A:18
PRO A:21
GLN A:19
ARG A:254
PRO A:20
VAL A:41
ASN A:14
PRO A:42
THR A:196
VAL A:244
ARG A:471
TRP A:194

Fig. 4 The 3D and 2D interactions with the hydrogen bond surface of **6f** (**A**) and crystallized compound (**B**) in complex with 4GQR.The 3D and 2D interactions with the hydrogen bond surface of **6b** (**C**) and crystallized compound (**D**) in complex with 3L4Y

interactions [52]. In this work, the 3D MEP surface of the studied molecule is created under gas-phase conditions, as shown in Fig. 8. Areas colored red indicate regions with higher electron density, which are more prone to electrophilic attack, while blue zones represent electron-deficient regions, favoring nucleophilic interactions. Neutral zones generally appear green. In most of the studied compounds, the deep red regions localized over the sulphonate moiety, suggesting favorable sites for electrophilic attack, while the blue-shaded regions near the hydrogen of thiosemicarbazones point toward likely nucleophilic attack sites.

Experimental

General

All chemicals and solvents utilized in this work were obtained from Sigma Aldrich and were of analytical grade with a purity of ≥ 98%. Dichloromethane (99%), nitric acid (99.9%), acetic acid (100%), triethylamine (99.5%), *N*, *N*-dimethylformamide (99.8%), methanol (99.9%), petroleum ether (99%), ethyl acetate (99%), 4-hydroxybenzaldehyde (98%), quinoline-8-sulfonyl chloride (98%) were used as received without further purification. Reaction progress and completion are monitored using TLC plates with aluminum backing. The Gallen-Kamp melting point apparatus is used to record melting points. A Bruker Ascend 400 MHz spectrometer is used to get ^{1}H and ^{13}C-NMR spectra in deuterated solvents like DMSO-d_6 (400 MHz for ^{1}H and 101 MHz for ^{13}C). Chemical shifts are reported in parts per million (ppm), and coupling constants (*J*) are given in Hertz (Hz) to describe signal multiplicity.

Synthesis of 4-hydroxy-3-nitrobenzaldehyde (2)

4-Hydroxy-3-nitrobenzaldehyde **(2)** is prepared following a previously reported method [53]. 4-Hydroxybenzaldehyde **(1)** (1 mmol) is added to 10 mL of DCM. HNO_3 (1 mmol) was added dropwise, and the mixture was sonicated for 30 min. The reaction progress is monitored by TLC, and the formation of yellow precipitates indicates the completion of the reaction. The resulting product is filtered, washed with water, and dried at room temperature.

Synthesis of 4-formyl-2-nitrophenyl quinoline-8-sulfonate (4)

4-Formyl-2-nitrophenyl quinoline-8-sulfonate **(4)** is prepared by following the reported method [53]. For the synthesis of 4-formyl-2-nitrophenyl quinoline-8-sulfonate **(4)**, 4-hydroxy-3-nitrobenzaldehyde **(2)** (3.425 mmol) and triethylamine (3.425 mmol) have been taken in a flask, and DMF (10 ml) is added while stirring in an ice bath. Quinoline-8-sulfonyl chloride **(3)** (3.425 mmol) is added, and the reaction is monitored by TLC. After 60 min, the reaction is quenched by adding distilled water (20 ml), resulting in the precipitation of the product. The precipitates are filtered and dried for further analysis.

Synthesis of thiosemicarbazones 6(a-i)

The required thiosemicarbazones **6(a-i)** are synthesized by reacting appropriate thiosemicarbazides **5(a-i)** (3.425 mmol) with compound **(4)** (3.425 mmol) in 10 ml of methanol, by adding a few drops of acetic acid. The mixture is refluxed at 65–70 °C for 3–6 h, and the reaction progress is monitored by TLC. The product is filtered, washed with methanol, and dried at room temperature. The synthesized compounds are characterized as follows:

(E)-4-{[2-((2,6-Dimethylphenyl)carbamothioyl) hydrazineylidene]methyl}-2-nitrophenyl quinoline-8-sulfonate (6a)

Yellow solid, m. p. 218–220 °C, Yield 82%. ^{1}H NMR (400 MHz, DMSO) δ 11.97 (s, 1H), 10.02 (s, 1H), 9.05 (dd, *J* = 4.3, 1.7 Hz, 1H), 8.64 (dd, *J* = 9.7, 1.8 Hz, 2 H), 8.51 (dd, *J* = 8.3, 1.4 Hz, 1H), 8.42 (dd, *J* = 7.5, 1.4 Hz, 1H), 8.11 (s, 1H), 8.04 (dd, *J* = 8.6, 2.1 Hz, 1H), 7.83–7.76 (m, 2 H), 7.16–7.09 (m, 4 H), 2.16 (s, 6H). ^{13}C NMR (101 MHz, DMSO) δ 177.5, 152.8, 143.9, 143.3, 141.4, 139.0, 137.6, 137.4, 137.3, 136.8, 134.8, 134.4, 133.5, 131.7, 129.3, 128.1, 127.5, 126.2, 124.9, 123.6, 123.5, 18.4.

(E)-2-Nitro-4-{[2-(o-Tolylcarbamothioyl)hydrazineylidene] methyl}phenyl quinoline-8-sulfonate (6b)

Yellow solid, m. p. 222–224 °C, Yield 75%. ^{1}H NMR (400 MHz, DMSO) δ 12.00 (s, 1H), 10.13 (s, 1H), 9.04 (dd, *J* = 4.2, 1.8 Hz, 1H), 8.63 (m, 2 H), 8.51 (dd, *J* = 8.2, 1.4 Hz, 1H), 8.43 (dd, *J* = 7.4, 1.4 Hz, 1H), 8.12 (s, 1H), 8.05 (dd, *J* = 8.7, 2.1 Hz, 1H), 7.83–7.77 (m, 2 H), 7.30–7.20 (m, 4 H), 7.16 (d, *J* = 8.6 Hz, 1H), 2.20 (s, 3 H). ^{13}C NMR (101 MHz, DMSO) δ 177.7, 152.8, 143.9, 143.3, 141.4, 139.2, 138.4, 137.6, 137.3, 136.2, 134.8, 134.4, 133.5, 131.7, 130.6, 129.4, 129.3, 127.4, 126.5, 126.2, 124.9, 123.6, 18.2.

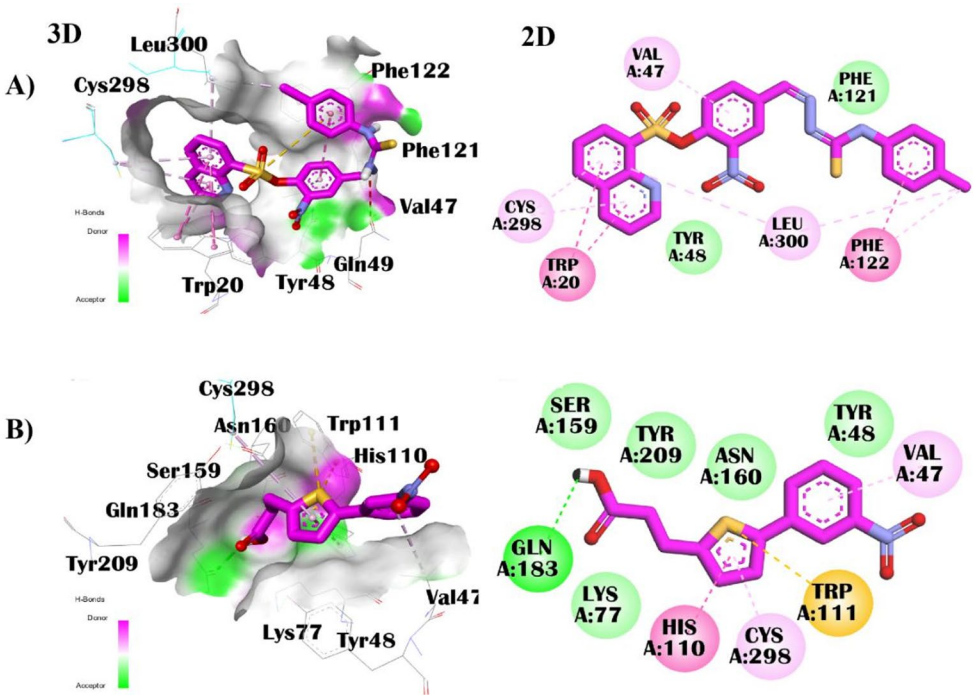

Fig. 5 The 3D and 2D interactions with the hydrogen bond surface of **6f** (**A**) and crystallized ligand (**B**) in complex with 4YU1

Table 3 The ADMET parameters for thiosemicarbazone derivatives and co-crystallized ligands of targeted proteins

Codes	TPSA	SlogP	logS	HIA	BBB	Pgp inhibitor	CYP3A4 inhibitor	CYP2D6 inhibitor
6a	135.82	4.85	−5.74	0.88	0.44	0.93	0.87	0.20
6b	135.82	4.54	−5.67	0.88	0.43	0.92	0.88	0.20
6c	135.82	4.23	−5.61	0.88	0.44	0.92	0.89	0.21
6d	135.82	4.04	−5.83	0.90	0.48	0.95	0.86	0.19
6e	135.82	5.54	−6.23	0.86	0.40	0.93	0.81	0.15
6f	135.82	4.89	−6.02	0.90	0.50	0.93	0.84	0.18
6g	135.82	2.34	−5.28	0.90	0.64	0.84	0.93	0.20
6h	135.82	4.22	−5.50	0.88	0.47	0.91	0.89	0.24
6i	178.96	4.14	−5.47	0.83	0.38	0.87	0.84	0.18
Co-4GQR	151.59	1.69	−3.09	0.59	0.04	0.28	0.25	0.46
Co-3L4Y	228.27	−6.02	−0.17	0.07	0.16	0.04	0.01	0.01
Co-4YU1	80.44	3.34	−4.16	0.98	0.60	0.34	0.02	0.05

(E)-2-Nitro-4-{[2-(Phenylcarbamothioyl)hydrazineylidene] methyl}phenyl quinoline-8-sulfonate (6c)

Yellow solid, m. p. 220–222 °C, Yield 85%. ^{1}H NMR (400 MHz, DMSO) δ 12.04 (s, 1H), 10.25 (s, 1H), 9.03 (dd, *J* = 4.2, 1.8 Hz, 1H), 8.65–8.60 (m, 2 H), 8.51 (dd, *J* = 8.3, 1.4 Hz, 1H), 8.43 (dd, *J* = 7.5, 1.4 Hz, 1H), 8.14 (s, 1H), 8.10 (dd, *J* = 8.7, 2.1 Hz, 1H), 7.84–7.76 (m, 2 H), 7.50–7.47 (m, 2 H), 7.38 (t, *J* = 7.8 Hz, 2 H), 7.26–7.21 (m, 1H), 7.18 (d, *J* = 8.6 Hz, 1H). ^{13}C NMR (101 MHz, DMSO) δ 177.0, 152.8, 143.8, 143.3, 141.6, 139.6, 139.4, 137.6, 137.3, 134.6, 134.4, 133.4, 131.7, 129.3, 128.6, 126.9, 126.2, 126.2, 124.9, 123.9, 123.6.

(E)-4-{[2-(Cyclohexylcarbamothioyl)hydrazineylidene] methyl}-2-nitrophenyl quinoline-8-sulfonate (6d)

Yellow solid, m. p. 268–270 °C, Yield 78%. ^{1}H NMR (400 MHz, DMSO) δ 11.72 (s, 1H), 9.66 (dd, *J* = 6.0, 1.7 Hz, 1H), 9.59 (dd, *J* = 8.3, 1.6 Hz, 1H), 8.87 (dd, *J* = 7.5, 1.7 Hz, 1H), 8.65–8.58 (m, 2 H), 8.41–8.32 (m, 3 H), 8.25 (s, 1H), 8.06 (t, *J* = 7.8 Hz, 1H), 7.88 (d, *J* = 8.3 Hz, 1H), 4.21 (dd, *J* = 11.8, 8.2 Hz, 1H), 1.94–1.86 (m, 2 H), 1.75 (d, *J* = 12.8 Hz, 2 H), 1.62 (d, *J* = 12.6 Hz, 1H), 1.55–1.41 (m, 2 H), 1.37–1.23 (m, 2 H), 1.15 (t, *J* = 12.5 Hz, 1H). ^{13}C NMR (101 MHz, DMSO) δ 176.5, 155.1, 151.6, 144.9, 140.0, 139.6, 139.3, 138.0, 137.3, 136.7, 133.7, 133.6, 131.7, 129.7, 123.4, 122.0, 32.1, 25.4.

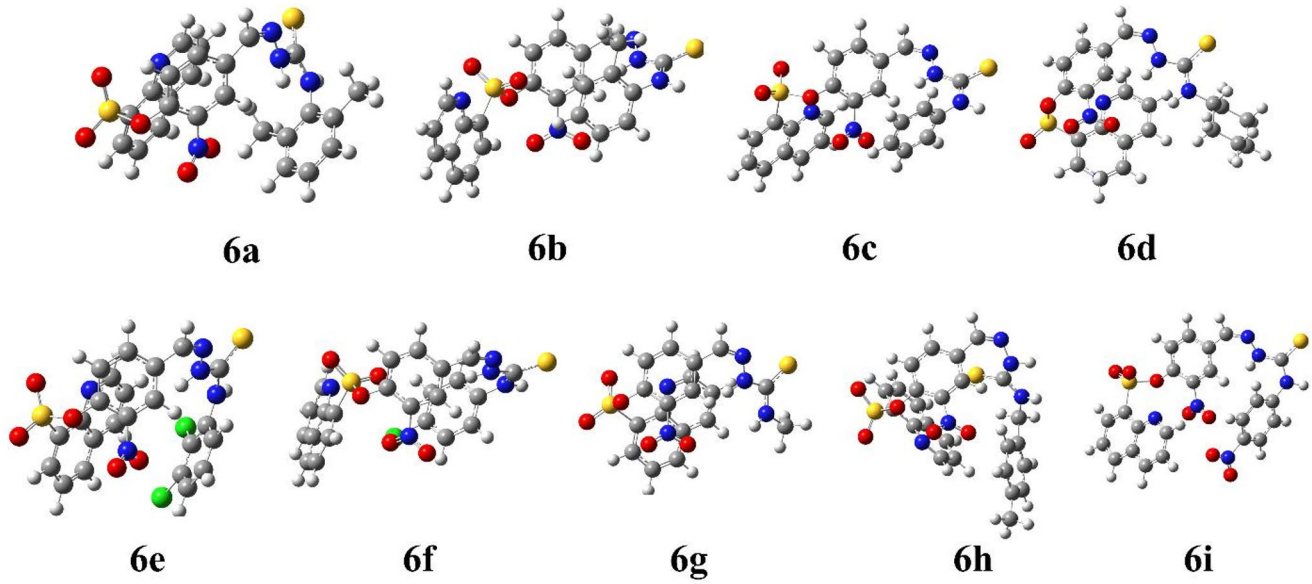

Fig. 6 Optimized structures of the studied compounds at DFT/B3LYP/6-311G(d, p)/GD3 calculations in the gas phase

Table 4 Energetic parameters of top hits using DFT/B3LYP/6-311G(d, p)/GD3 in the S_0 gas phase

Codes	Optimization energy (a.u.)	Dipole Moment (Debye)	Polarizability (a.u.)	HOMO (eV)	LUMO (eV)	HOMO-LUMO(Δ eV)
6a	−2411.92	4.74	386.94	−6.022	−3.100	2.922
6b	−2372.58	11.02	390.95	−5.622	−3.211	2.411
6c	−2333.26	8.05	375.83	−5.658	−3.120	2.538
6d	−2336.90	5.00	370.96	−5.86	−3.24	2.61
6e	−3252.50	3.29	393.83	−6.222	−3.203	3.020
6f	−2792.88	8.91	389.79	−5.688	−3.269	2.419
6g	−2141.46	4.24	309.35	−6.078	−3.255	2.823
6h	−2411.91	8.70	381.54	−6.237	−2.815	3.422
6i	−2537.82	3.58	417.17	−6.309	−3.183	3.125

(E)-4-{[2-((2,3-Dichlorophenyl)carbamothioyl) hydrazineylidene]methyl}-2-nitrophenyl quinoline-8-sulfonate (6e)

Yellow solid, m. p. 215–217 °C, Yield 88%. ^{1}H NMR (500 MHz, DMSO) δ 12.27 (s, 1H), 10.32 (s, 1H), 9.04 (dd, *J*=4.2, 1.8 Hz, 1H), 8.65–8.61 (m, 2 H), 8.51 (dd, *J*=8.2, 1.4 Hz, 1H), 8.44 (dd, *J*=7.5, 1.4 Hz, 1H), 8.16 (s, 1H), 8.08 (dd, *J*=8.7, 2.0 Hz, 1H), 7.85–7.77 (m, 2 H), 7.62 (dd, *J*=8.1, 1.6 Hz, 1H), 7.53 (dd, *J*=8.0, 1.5 Hz, 1H), 7.43 (d, *J*=8.1 Hz, 1H), 7.20 (d, *J*=8.6 Hz, 1H). ^{13}C NMR (126 MHz, DMSO) δ 177.8, 152.8, 143.8, 143.3, 141.7, 140.0, 140.0, 139.1, 137.6, 137.3, 134.5, 134.4, 133.6, 132.2, 131.7, 131.0, 130.1, 129.3, 128.2, 126.2, 125.1, 123.8, 123.6.

(E)-4-{[2-((4-Chlorophenyl)carbamothioyl) hydrazineylidene]methyl}-2-nitrophenyl quinoline-8-sulfonate (6f)

Yellow solid, m. p. 243–245 °C, Yield 85%. ^{1}H NMR (400 MHz, DMSO) δ 12.12 (s, 1H), 10.27 (s, 1H), 9.03 (dd, *J*=4.2, 1.7 Hz, 1H), 8.64 (dd, *J*=8.3, 1.7 Hz, 1H), 8.60 (d, *J*=2.1 Hz, 1H), 8.52 (dd, *J*=8.4, 1.4 Hz, 1H), 8.43 (dd, *J*=7.5, 1.4 Hz, 1H), 8.15 (s, 1H), 8.11 (dd, *J*=8.7, 2.1 Hz, 1H), 7.84–7.77 (m, 2 H), 7.54 (d, *J*=8.8 Hz, 2 H), 7.45–7.42 (m, 2 H), 7.18 (d, *J*=8.6 Hz, 1H).

(E)-4-{[2-(Methylcarbamothioyl)hydrazineylidene]methyl}-2-nitrophenyl quinoline-8-sulfonate (6g)

Yellow solid, m. p. 254–256 °C, Yield 79%. ^{1}H NMR (400 MHz, DMSO) δ 11.72 (s, 1H), 9.03 (dd, *J*=4.2, 1.8 Hz, 1H), 8.70 (d, *J*=4.8 Hz, 1H), 8.64 (dd, *J*=8.4, 1.7 Hz, 1H), 8.53–8.49 (m, 2 H), 8.43 (dd, *J*=7.5, 1.4 Hz, 1H), 8.03 (s, 1H), 8.00 (dd, *J*=8.7, 2.1 Hz, 1H), 7.84–7.77 (m, 2 H), 7.17 (d, *J*=8.6 Hz, 1H), 3.01 (d, *J*=4.5 Hz, 3 H). ^{13}C NMR (101 MHz, DMSO) δ 178.3, 152.8, 143.8, 143.3, 141.4, 138.4, 137.6, 137.3, 134.9, 134.4, 133.0, 131.7, 129.3, 126.2, 125.0, 123.6, 123.5, 31.3.

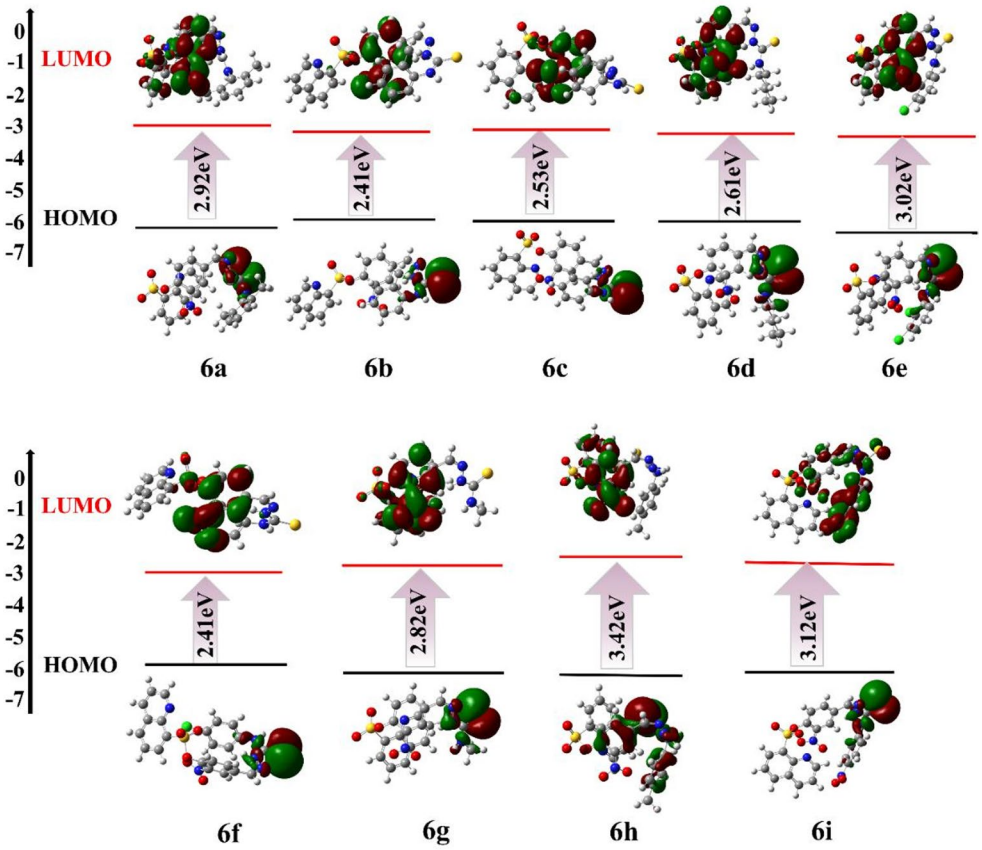

Fig. 7 HOMO/LUMO contour Maps of the studied compounds at DFT/B3LYP/6–311 g(d, p)/GD3 calculations in the gas phase

Table 5 The quantum chemical descriptors for top hits using DFT/B3LYP/6–311 g(d, p)/GD3 in the S_0 gas phase

Codes	Chemical potential μ (eV)	Electro-negativity χ (eV)	Chemical hardness η (eV)	Chemical softness ζ (eV)	Electrophilicity index ω (eV)	Ionization potential I (eV)	Electron affinity A (eV)
6a	−4.561	4.561	1.461	0.342	7.119	6.022	3.100
6b	−4.417	4.417	1.205	0.415	8.091	5.622	3.211
6c	−4.389	4.389	1.269	0.394	7.590	5.658	3.120
6d	−4.551	4.551	1.309	0.382	7.912	5.861	3.242
6e	−4.713	4.713	1.510	0.331	7.355	6.222	3.203
6f	−4.478	4.478	1.209	0.413	8.291	5.688	3.269
6g	−4.666	4.666	1.412	0.354	7.712	6.078	3.255
6h	−4.526	4.526	1.711	0.292	5.986	6.237	2.815
6i	−4.746	4.746	1.563	0.320	7.208	6.309	3.183

(E)-4-{[2-((4-Methylbenzyl)carbamothioyl) hydrazineylidene]methyl}-2-nitrophenyl quinoline-8-sulfonate (6h)

Yellow solid, m. p. 212–214 °C, Yield 83%. ^{1}H NMR (400 MHz, DMSO) δ 11.80 (s, 1H), 9.22 (t, *J* = 6.2 Hz, 1H), 9.03 (dd, *J* = 4.3, 1.8 Hz, 1H), 8.63 (dd, *J* = 8.4, 1.8 Hz, 1H), 8.52–8.48 (m, 2 H), 8.42 (dd, *J* = 7.5, 1.4 Hz, 1H), 8.07 (s, 1H), 8.02 (dd, *J* = 8.7, 2.2 Hz, 1H), 7.83–7.76 (m, 2 H), 7.20 (d, *J* = 7.9 Hz, 2 H), 7.13 (t, *J* = 8.3 Hz, 3 H), 4.79 (d, *J* = 6.2 Hz, 2 H), 2.27 (s, 3 H). ^{13}C NMR (101 MHz, DMSO) δ 178.2, 152.8, 143.8, 143.3, 141.4, 139.0, 137.6, 137.3, 136.5, 136.2, 134.8, 134.4, 133.0, 131.7, 129.3, 129.1, 127.5, 126.2, 125.0, 123.7, 123.6, 46.8, 21.1.

(E)-2-Nitro-4-{[2-((4-Nitrophenyl)carbamothioyl) hydrazineylidene]methyl}phenyl quinoline-8-sulfonate (6i)

Yellow solid, m. p. 228–230 °C, Yield 81%. ^{1}H NMR (400 MHz, DMSO) δ 12.38 (s, 1H), 10.52 (s, 1H), 9.03 (dd, *J* = 4.2, 1.8 Hz, 1H), 8.64 (dd, *J* = 8.4, 1.8 Hz, 1H), 8.60 (d, *J* = 2.1 Hz, 1H), 8.52 (dd, *J* = 8.3, 1.4 Hz, 1H), 8.44 (dd, *J* = 7.5, 1.4 Hz, 1H), 8.27–8.24 (m, 2 H), 8.20 (s, 1H), 8.15 (dd, *J* = 8.6, 2.1 Hz, 1H), 8.01–7.98 (m, 2 H), 7.84–7.77 (m,

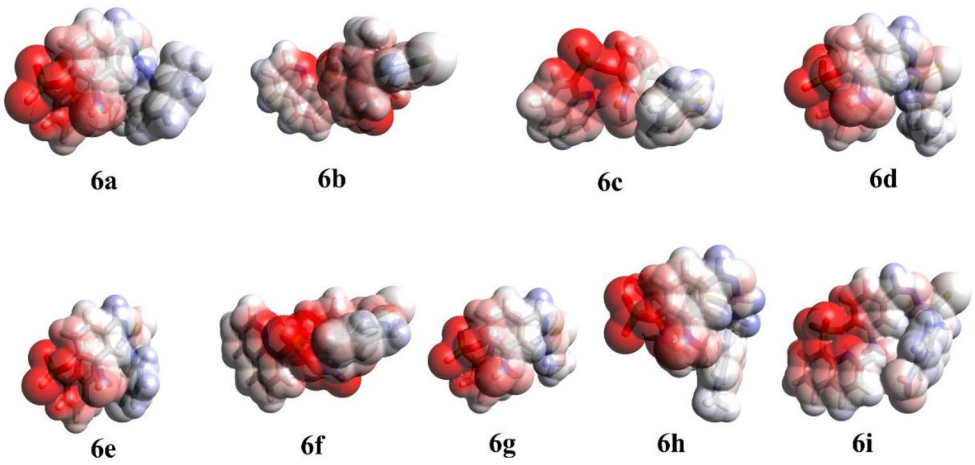

Fig. 8 MEP maps for the studied compounds at B3LYP/6–311 g(d, p)/GD3 level of theory in the gas phase

2 H), 7.22 (d, J = 8.6 Hz, 1H). ^{13}C NMR (101 MHz, DMSO) δ 176.3, 152.8, 145.6, 144.2, 143.8, 143.3, 141.9, 140.9, 137.6, 137.3, 134.4, 134.2, 133.5, 131.7, 129.3, 126.2, 125.5, 125.1, 124.3, 124.2, 123.6.

Molecular docking

The series of thiosemicarbazone derivatives is analyzed for the inhibition of α-Amylase, α-Glucosidase, and Aldose-reductase with PDB IDs of 4GQR, 3L4Y, and 4YU1, respectively, proteins, by docking simulation. The 3D crystal structures are retrieved from PDB-RCSB and are prepared by AutoDockTools-1.5.7. The non-protein parts are removed from the .pdb files of each protein, to ensure that the target proteins do not contain any ligand molecule before docking [54]. The Kollman charges and polar hydrogen atoms are incorporated into the protein structure to model key interactions between the receptor-ligated complex [55]. The thiosemicarbazone derivatives are initially drawn in ChemDraw 20.1.1 [56, 57] and subsequently subjected to energy minimization using Chem3D 20.1.1 [58] to obtain a reliable structural conformation. The optimized compounds and 3D protein structures are converted to .pdbqt format by AutoDockTools-1.5.7 [59, 60], to execute the docking simulations. The grid maps, necessary for docking protocol, are identified by binding coordinates of the co-crystallized ligand within the pocket of respective proteins. The RMSD (root mean square deviation) value of the redocked crystallized ligand is calculated to validate docking simulation accuracy [61].

Quantum computational methodology

The geometric structure of the investigated compounds is optimized using density DFT with the B3LYP functional and 6-311G(d, p) basis set. All calculations are conducted using Gaussian 16 software, and the optimized geometry is analyzed through GaussView 6.0 [62]. To explore the electronic characteristics of the molecule, frontier molecular orbitals such as HOMO and LUMO are visualized, providing insight into electron distribution and potential charge transfer within the system. The global reactivity descriptors such as ionization potential (I), electron affinity (A), electronegativity (χ), chemical hardness (η), chemical potential (μ), and electrophilicity index (ω) are measured based on frontier orbital energies, using Koopmans' theorem [59, 51]. These parameters serve as predictive indicators of the molecule's chemical reactivity, stability, and possible interaction behavior. Furthermore, the molecular electrostatic potential surface is mapped to determine regions susceptible to electrophilic and nucleophilic attack, offering a spatial understanding of reactive centers [63]. The MEP maps are visualized in Avogadro software.

Conclusion

In this study, a novel series of 4-formyl-2-nitrophenyl quinoline-8-sulfonate-based thiosemicarbazone derivatives **6(a-i)** is rationally designed as potential antidiabetic agents. Their biological efficacy is assessed through α-amylase and α-glucosidase inhibition assays, where all synthesized compounds demonstrated notable inhibition potential, with IC_{50} values ranging from 9.66 to 169.71 μM. The combined results from DFT calculations and molecular docking studies offer a coherent understanding of the electronic behavior and binding potential of the investigated compounds. Theoretical analysis revealed that the HOMO-LUMO energy gaps varied between 2.41 and 3.42 eV, indicating differences in molecular reactivity and stability across the series. Compounds with narrower band gaps showed lower chemical hardness and higher electrophilicity, suggesting a greater tendency to interact with biological targets. The findings are further supported by molecular docking studies, where **6b**

and **6f**, with smaller ΔE values, demonstrated stronger binding affinities with docking energies of − 9.1 and − 10.4 kcal/mol, respectively. Additionally, the studied compounds exhibiting higher dipole moments (up to 11.02 D) and polarizability values (above 400 a.u.) tended to align better within the active site, thereby forming key interactions such as hydrogen bonds and π-π stacking. These observations highlight a meaningful correlation between electronic descriptors from DFT and binding behavior observed in docking simulations, supporting the role of frontier orbital properties and electrostatic features in governing biological activity.

Supplementary Information The online version contains supplementary material available at https://doi.org/10.1007/s10822-025-00707-z.

Acknowledgements The authors extend their appreciation to the Deanship of Research and Graduate Studies at King Khalid University, Saudi Arabia, through the Large Research Project under grant number RGP-2/684/46. K.M. is thankful to HEC, Pakistan for the award of NRPU, Project No. 10525/Punjab/NRPU/R&D/HEC/2017 by Higher Education Commission (HEC), Islamabad, Pakistan.

Author contributions Investigation: M.T., K.A., and M.B. Formal Analysis, Data curation: N.H., H.S., and X.Z. Methodology, Software: P.T., K.M. Funding acquisition, Resources, Validation: M.A.I., A.K.A. Conceptualization, Supervision, Writing original draft: M.T., F.S., and Z.S.

Funding The authors extend their appreciation to the Deanship of Research and Graduate Studies at King Khalid University, Saudi Arabia, through the Large Research Project under grant number RGP-2/684/46.

Data availability The data supporting this article have been included as part of the ESI.

Declarations

Competing interests The authors declare no competing interests.

References

1. Hossain U, Das AK, Ghosh S, Sil PC (2020) An overview on the role of bioactive α-glucosidase inhibitors in ameliorating diabetic complications. Food Chem Toxicol 145:111738
2. Safiri S, Karamzad N, Kaufman JS, Bell AW, Nejadghaderi SA, Sullman MJ, Moradi-Lakeh M, Collins G, Kolahi A-A (2022) Prevalence, deaths and disability-adjusted-life-years (DALYs) due to type 2 diabetes and its attributable risk factors in 204 countries and territories, 1990–2019: results from the global burden of disease study 2019. Front Endocrinol 13:838027
3. Kashtoh H, Baek K-H (2022) Recent updates on phytoconstituent alpha-glucosidase inhibitors: an approach towards the treatment of type two diabetes. Plants 11(20):2722
4. Dirir AM, Daou M, Yousef AF, Yousef LF (2022) A review of alpha-glucosidase inhibitors from plants as potential candidates for the treatment of type-2 diabetes. Phytochem Rev 21(4):1049–1079
5. Mushtaq A, Azam U, Mehreen S, Naseer MM (2023) Synthetic α-glucosidase inhibitors as promising anti-diabetic agents: recent developments and future challenges. Eur J Med Chem 249:115119
6. Gulçin İ, Taslimi P, Aygün A, Sadeghian N, Bastem E, Kufrevioglu OI, Turkan F, Şen F (2018) Antidiabetic and antiparasitic potentials: inhibition effects of some natural antioxidant compounds on α-glycosidase, α-amylase and human glutathione S-transferase enzymes. Int J Biol Macromol 119:741–746
7. Quattrin T, Mastrandrea LD, Walker LS (2023) Type 1 diabetes. Lancet 401(10394):2149–2162
8. Prajapati NP, Patel HD (2019) Novel thiosemicarbazone derivatives and their metal complexes: recent development. Synth Commun 49(21):2767–2804
9. Cheng X, Huang J, Li H, Zhao D, Liu Z, Zhu L, Zhang Z, Peng W (2024) Quercetin: a promising therapy for diabetic encephalopathy through Inhibition of hippocampal ferroptosis. Phytomedicine 126:154887
10. Peng Q, Zhang H, Li Z (2025) KAT2A-mediated H3K79 succinylation promotes ferroptosis in diabetic nephropathy by regulating SAT2. Life Sci 123746
11. Mi W, Xia Y, Bian Y (2019) The influence of ICAM1 rs5498 on diabetes mellitus risk: evidence from a meta-analysis. Inflamm Res 68(4):275–284
12. Zhang Y, Nie C, Wang Z, Lan F, Wan L, Li A, Zheng P, Zhu W, Pan Q (2025) A Spatial confinement biological heterogeneous cascade nanozyme composite hydrogel combined with nitric oxide gas therapy for enhanced treatment of psoriasis and diabetic wound. Chem Eng J 507:160629
13. Ullah N, Alam A, Tüzün B, Rehman NU, Ayaz M, Elhenawy AA, Khan A, Rahman SU, Ali M, Latif A (2025) Synthesis of novel thiazole derivatives containing 3-methylthiophene carbaldehyde as potent anti α-glucosidase agents: in vitro evaluation, molecular docking, dynamics, MM-GBSA, and DFT studies. J Mol Struct 1321:140070
14. Shakoor A, Fareed G, Ahmad I, Elhenawy AA, Khan M, Fareed N, Al-Olayan E, Abukhadra MR, Alam A, Ibrahim M (2025) Exploring the anti-diabetic activity of benzimidazole containing schiff base derivatives: in vitro α-amylase, α-glucosidase inhibitions and in Silico studies. J Mol Struct 1321:140136
15. Aftab H, Ullah S, Khan A, Al-Rashida M, Islam T, Alshammari A, Albekairi NA, Taslimi P, Al-Harrasi A, Shafiq Z (2024) Synthesis, in vitro biological evaluation and in silico studies of novel pyrrolidine derived thiosemicarbazones as dihydrofolate reductase inhibitors. RSC Adv 14(43):31409–31421
16. Pili R, Chang J, Partis RA, Mueller RA, Chrest FJ, Passaniti A (1995) The α-glucosidase I inhibitor castanospermine alters endothelial cell glycosylation, prevents angiogenesis, and inhibits tumor growth. Cancer Res 55(13):2920–2926
17. Zitzmann N, Mehta AS, Carrouée S, Butters TD, Platt FM, McCauley J, Blumberg BS, Dwek RA, Block TM (1999) Imino sugars inhibit the formation and secretion of bovine viral diarrhea virus, a pestivirus model of hepatitis C virus: implications for the development of broad spectrum anti-hepatitis virus agents. Proc Natl Acad Sci 96(21):11878–11882
18. Korkmaz G (2024) A review of recent research on the antimicrobial activities of thiosemicarbazone-based compounds. J New Results Sci 13(1):61–83
19. Pitucha M, Ramos P, Wojtunik-Kulesza K, Głogowska A, Stefańska J, Kowalczuk D, Monika D, Augustynowicz-Kopeć E (2023) Thermal analysis, antimicrobial and antioxidant studies of thiosemicarbazone derivatives. J Therm Anal Calorim 148(10):4223–4234
20. Farooqi R, Ullah S, Khan A, Gurav SS, Mali SN, Aftab H, Al-Sadoon MK, Hsu M-H, Al-Harrasi A, Shafiq Z, Design synthesis,

in-vitro and in-silico studies of novel N-heterocycle based hydrazones as A-glucosidase inhibitors. Available at SSRN 4962025
21. Alam M, Abser MN, Kumer A, Bhuiyan MMH, Akter P, Hossain ME, Chakma U (2023) Synthesis, characterization, antibacterial activity of thiosemicarbazones derivatives and their computational approaches: quantum calculation, molecular docking, molecular dynamic, ADMET, QSAR. Heliyon 9(6)
22. Hernández W, Carrasco F, Vaisberg A, Spodine E, Icker M, Krautscheid H, Beyer L, Tamariz-Angeles C, Olivera-Gonzales P (2023) Novel thiosemicarbazone derivatives from furan-2-carbaldehyde: synthesis, characterization, crystal structures, and antibacterial, antifungal, antioxidant, and antitumor activities. J Chem 2023(1):5413236
23. Zahra SB, Khan A, Ahmed N, Rafique M, Fatima L, Khan I, Hussain J, Khalid S, Ogaly HA, Ahmed MM (2025) Versatile biological activities of thiosemicarbazones and their metal complexes. J Mol Struct 1322:140511
24. Batool Z, Dutt SM, al-Rashida M, Gelsleichter NE, Pelletier J, Sévigny J, Islam T, Aftab H, Almutairi TM, Çakır F (2025) N-hexylsulfonyl Indole based thiosemicarbazones as potent and selective ecto-5′-nucleotidase and NTPDase inhibitors. Bioorg Chem 108717
25. Aftab H, Ullah S, Khan A, Al-Rashida M, Islam T, Dahlous KA, Mohammad S, Kashtoh H, Al-Harrasi A, Shafiq Z (2024) Design, synthesis, in vitro and in Silico studies of novel piperidine derived thiosemicarbazones as inhibitors of dihydrofolate reductase. Sci Rep 14(1):22645
26. Kumar B, Devi J, Dubey A, Tufail A, Sharma S (2024) Exploring the antimalarial, antioxidant, anti-inflammatory activities of newly synthesized transition metal (II) complexes bearing thiosemicarbazone ligands: insights from molecular docking, DFT, MESP and ADMET studies. Inorg Chem Commun 159:111674
27. Farghaly TA, Abbas EM, Abd-Elghaffar HS, Elsayed MA, Elnaggar DH, El-Sayed AF, Abd-Elshafy DN, Mohamed SF (2024) Synthesis, characterization, molecular docking, pharmacokinetics, and molecular dynamics of new bis-thiazoles based on bis-thiosemicarbazone as anti-coxsackievirus. Sci Rep 14(1):29378
28. Idris S, Jan F, Waheed M, Alam A, Ibrahim M, Alasmari AF, Alasmari F, Bo L, Khan M (2024) Multifaceted bioactivity of thiosemicarbazide derivatives: synthesis, characterization, and DFT investigations on Inhibition of α-amylase, hydroxyl radical scavenging, and iron chelating activities with molecular docking insights. J Mol Struct 1304:137669
29. Shoukat W, Hussain M, Ali A, Shafiq N, Chughtai AH, Shakoor B, Moveed A, Shoukat MN, Milošević M, Mohany M, Design (2025) Synthesis, characterization and biological screening of novel thiosemicarbazones and their derivatives with potent antibacterial and antidiabetic activities. J Mol Struct 1320:139614
30. Jan F, Idris S, Waheed M, Alam A, Alasmari AF, Alasmari F, Khan M (2024) Thiosemicarbazone derivatives as potent antidiabetic agents: synthesis, in vitro, molecular docking and DFT investigations. J Mol Struct 1311:138459
31. Waheed M, Idris S, Jan F, Alam A, Ibrahim M, AlAsmari AF, Alharbi M, Alasmari F, Khan M (2023) Exploring the synthesis, structure, spectroscopy and biological activities of novel 4-benzylidene-1-(2-(2, 4-dichloro phenyl) acetyl) Thiosemicarbazide derivatives: an integrated experimental and theoretical investigation. Saudi Pharm J 31(12):101874
32. Ullah N, Alam A, Zainab; Elhenawy AA, Naz S, Islam MS, Ahmad S, Shah SAA, Ahmad M (2024) Investigating novel thiophene carbaldehyde based thiazole derivatives as potential hits for diabetic management: synthesis, in vitro and in Silico approach. ChemistrySelect 9(8):e202304601
33. Rahman SU, Alam A, Parveen Z, Assad M, Shah SAA, Rafiq H, Ayaz M, Latif A, Umar MN, Ali M (2024) Novel acyl Hydrazide derivatives of polyhydroquinoline as potent anti-diabetic and anti-glycating agents: synthesis, in vitro α-amylase, α-glucosidase Inhibition and anti-glycating activity with molecular docking insights. Bioorg Chem 150:107501
34. Talab F, Zainab; Alam A, Ali M, Rehman NU, Ullah S, Halim SA, Islam MS, Khan A, Latif A (2023) Polyhydroquinoline derivatives for diabetic management: synthesis, in vitro and in Silico approaches. Future Med Chem 15(23):2195–2208
35. Gul S, Elhenawy AA, Ali Q, Rehman MU, Alam A, Khan M, AlAsmari AF, Alasmari F (2024) Discovering the anti-diabetic potential of thiosemicarbazone derivatives: in vitro α-glucosidase, α-amylase inhibitory activities with molecular docking and DFT investigations. J Mol Struct 1312:138671
36. Khan M, Gohar H, Alam A, Wadood A, Shareef A, Ali M, Khalid A, Abdalla AN, Ullah F (2023) Para-substituted thiosemicarbazones as cholinesterase inhibitors: synthesis, in vitro biological evaluation, and in silico study. ACS Omega 8(5):5116–5123
37. Essid M, Alam A, Fareed G, Rahman S, Ahmad I, Zghab I, Alnakhli ZH, Ali A, Kamal M, Khan M (2025) Discovering the cholinesterase inhibitory potential of thiosemicarbazone derivatives through in vitro, molecular docking, kinetics, and dynamics studies. Med Chem (Shariqah (United Arab Emirates))
38. Alharthy RD, Khalid S, Fatima S, Ullah S, Khan A, Mali SN, Jawarkar RD, Dhabarde SS, Kashtoh H, Taslimi P (2024) Synthesis of the chromone-thiosemicarbazone scaffold as promising α-glucosidase inhibitors: an in vitro and in silico approach toward antidiabetic drug design. Arch Pharm e2400140
39. Ullah H, Khan S, Rahim F, Taha M, Iqbal R, Sarfraz M, Shah SAA, Sajid M, Awad MF, Omran A (2022) Benzimidazole bearing thiosemicarbazone derivatives act as potent α-amylase and α-glucosidase inhibitors; synthesis, bioactivity screening and molecular docking study. Molecules 27(20):6921
40. Şahin H, Bingül AA, Şengül İF, Bingül M (2023) Biological and computational evaluation of carbazole-based bis-thiosemicarbazones: a selective enzyme Inhibition study between α-amylase and α-glucosidase. İstanbul J Pharm 53(1):39–44
41. Korkmaz A, Bursal E, Kurtay G (2023) In vitro and in silico evaluation of amylase, tyrosinase, and pancreatic lipase inhibitions of novel benzothiazole-sulfonate derivatives. ChemistrySelect 8(42):e202302936
42. Mokoena TP, Maluleka MM, Mampa RM, Mphahlele MJ, Monchusi BA (2023) Synthesis, crystal structures, spectroscopic characterization and in vitro evaluation of the 4-sulfono-3-methoxycinnamaldehydes as potential α-glucosidase and/or α-amylase inhibitors. J Mol Struct 1271:134119
43. Shen C, Yang M, Xu J, Chen C, Zheng K, Shen J, Zhang P (2017) Iodobenzene-catalyzed synthesis of Aryl sulfonate esters from aminoquinolines via remote radical C–O cross-coupling. RSC Adv 7(78):49436–49439
44. Bisz E (2021) Iron-catalyzed cross-coupling reactions of alkyl grignards with aryl chlorobenzenesulfonates. Molecules 26(19):5895
45. Şenkardeş S, İhsan Han M, Gürboğa M, Özakpinar ÖB (2022) Güniz Küçükgüzel, Ş. Synthesis and anticancer activity of novel hydrazone linkage-based Aryl sulfonate derivatives as apoptosis inducers. Med Chem Res 31(2):368–379
46. Kamalı A, Çakmak R, Boğa M (2022) Anticholinesterase and antioxidant activities of novel heterocyclic schiff base derivatives containing an Aryl sulfonate moiety. J Chin Chem Soc 69(4):731–743
47. Kurban MG, Çakmak R, Başaran E, Türkmenoğlu B, Şentürk M (2024) Synthesis of new sulfonamide derivatives: investigation of their interactions with carbonic anhydrase and cholinesterase enzymes by in vitro and in Silico evaluations. J Mol Struct 138798

48. Cheng F, Li W, Zhou Y, Shen J, Wu Z, Liu G, Lee PW, Tang Y (2012) admetSAR: a comprehensive source and free tool for assessment of chemical ADMET properties. ACS Publications
49. Gu Y, Yu Z, Wang Y, Chen L, Lou C, Yang C, Li W, Liu G, Tang Y (2024) admetSAR3. 0: a comprehensive platform for exploration, prediction and optimization of chemical ADMET properties. Nucleic Acids Res 52(W1):W432–W438
50. Hou T, Xu X (2003) ADME evaluation in drug discovery. 3. Modeling blood-brain barrier partitioning using simple molecular descriptors. J Chem Inf Comput Sci 43(6):2137–2152
51. Arshad M, Ahmed K, Bashir M, Kosar N, Kanwal M, Ahmed M, Khan HU, Khan S, Rauf A, Waseem A (2021) Synthesis, structural properties and potent bioactivities supported by molecular docking and DFT studies of new hydrazones derived from 5-chloroisatin and 2-thiophenecarboxaldehyde. J Mol Struct 1246:131204
52. Ahmed K, Bashir M, Bano R, Sarfraz M, Khan HU, Khan S, Sharif A, Waseem A, Gilani MA, Batool K (2023) Potent heteroaromatic hydrazone based 1, 2, 4-triazine motifs: synthesis, anti-oxidant activity, cholinesterase inhibition, quantum chemical and molecular docking studies. J Mol Struct 1284:135383
53. Korkmaz A, Bursal E (2022) Synthesis, biological activity and molecular docking studies of novel sulfonate derivatives bearing salicylaldehyde. Chem Biodivers 19(6):e202200140
54. Mendie LE, Hemalatha S (2022) Molecular docking of phytochemicals targeting GFRs as therapeutic sites for cancer: an in Silico study. Appl Biochem Biotechnol 194(1):215–231
55. using AutoDock D Ethyl acetate extract of smilax glabra Roxb roots and its major active compound Astilbin promote osteoblastogenesis in vitro by upregulating bone cell differentiation-associated genes
56. Saxena AK, Gupta AK, Bhatia KS (2024) Physicochemical significance of ChemDraw and Dragon computed parameters: correlation studies in the sets with aliphatic and aromatic substituents. J Math Chem 62(10):2430–2455
57. Lakshmanan K, Balasubramanian HB, Aiyalu R, Ramasamy A (2019) Molecular Docking studies of flavones in Gentianaceae family against liver corrective targets. Res J Pharmacogn Phytochem 11(2):49–53
58. Sarfraz M, Aziz M, Afzal S, Channar PA, Alsfouk BA, Kandhro GA, Hassan S, Sultan A, Hamad A, Arafat M (2024) Repurposing of strychnine as the potential inhibitors of Aldo–keto reductase family 1 members B1 and B10: computational modeling and Pharmacokinetic analysis. Protein J 43(2):207–224
59. Siddique F, Daoui O, Ayoub M, Elkhattabi S, Chtita S, Afzal S, Mohyuddin A, Kaukab I, Ejaz SA, Salamatullah AM (2024) Identification and in silico screening of natural phloroglucinols as potential PI3Kα inhibitors: a computational approach for drug discovery. Open Chem 22(1):20240064
60. Kameswaran S, Swapna B, Ramakrishna M, Ramesh B, Bangeppagari M (2024) Different tools for modern drug discovery research. In: Traditional resources and tools for modern drug discovery: ethnomedicine and Pharmacology. Springer, pp 55–76
61. da Fonseca AM, Caluaco BJ, Madureira JMC, Cabongo SQ, Gaieta EM, Djata F, Colares RP, Neto MM, Fernandes CFC, Marinho GS (2024) Screening of potential inhibitors targeting the main protease structure of SARS-CoV-2 via molecular docking, and approach with molecular dynamics, RMSD, RMSF, H-bond, SASA and MMGBSA. Mol Biotechnol 66(8):1919–1933
62. Bilal MS, Ejaz SA, Zargar S, Akhtar N, Wani TA, Riaz N, Aborode AT, Siddique F, Altwaijry N, Alkahtani HM (2022) Computational investigation of 1, 3, 4 oxadiazole derivatives as lead inhibitors of VEGFR 2 in comparison with EGFR: density functional theory, molecular Docking and molecular dynamics simulation studies. Biomolecules 12(11):1612
63. Noor S, Aljasir MA, Bashir M, Khan K, Ahmad S, Abideen SA, Khan S, Siddique F, Ahmad H, Ghani K (2025) Multi-scale computational modeling to identify novel chemical scaffolds as trehalose-6-phosphate phosphatase inhibitors to combat burkholderia Pseudomallei. Silico Pharmacol 13(1):21